

ADVANCED MATERIALS

Supporting Information

for *Adv. Mater.*, DOI: 10.1002/adma.202205226

Chemical Vapor Deposition of High-Optical-Quality
Large-Area Monolayer Janus Transition Metal
Dichalcogenides

*Ziyang Gan, Ioannis Paradisanos, Ana Estrada-Real,
Julian Picker, Emad Najafidehaghani, Francis Davies,
Christof Neumann, Cedric Robert, Peter Wiecha, Kenji
Watanabe, Takashi Taniguchi, Xavier Marie, Johannes
Biskupek, Manuel Mundsztzinger, Robert Leiter, Ute
Kaiser, Arkady V. Krasheninnikov, Bernhard Urbaszek,*
Antony George,* and Andrey Turchanin**

Supporting Information

Chemical vapor deposition of high optical quality large area monolayer Janus transition metal dichalcogenides

Ziyang Gan†, Ioannis Paradisanos†, Ana Estrada-Real†, Julian Picker, Emad Najafidehaghani, Francis Davies, Christof Neumann, Cedric Robert, Peter Wiecha, Kenji Watanabe, Takashi Taniguchi, Xavier Marie, Johannes Biskupek, Manuel Mundsziinger, Robert Leiter, Ute Kaiser, Arkady V. Krashennnikov, Bernhard Urbaszek, Antony George*, Andrey Turchanin**

Supplementary Note 1: Methods

Synthesis of monolayer (ML) Janus SeMoS on Au foils

Polycrystalline Au foils (99.95 %, 250 μm thick, $1 \times 1 \text{ cm}^2$ size, Alfa Aesar) were used as growth substrates. They were initially ultrasonically cleaned in HCl solution (20 wt. %) for 15 min, followed by an acetone solution for 15 min. Then the cleaned Au foils were loaded into the CVD chamber and annealed at 1040 $^{\circ}\text{C}$ for over 10 h under the protection of the mixture gas of Ar/H₂ (200/10 cm^3/min) at ambient pressure. The annealing treatment reduces the surface roughness of Au foils and promotes their recrystallization toward (111) surface orientation,^[1] which is an epitaxial surface for TMD growth.^[1, 2]

The growth of ML Janus SeMoS was carried out in a three-zone split tube furnace (Carbolite Gero) with a quartz reaction tube of 60 mm diameter. An inner tube with a diameter of 15 mm was used to place the precursors and substrates (Figure S1). The three-zone configuration allowed to heat the Au foils together with the transition metal oxide precursor and chalcogen precursors (S and Se) individually. Knudsen-type effusion cells were used to deliver the chalcogen precursors.^[3, 4] As shown in Figure S1, the Knudsen cell loaded with S powder (99.98%, Sigma Aldrich) was placed on the first zone of the furnace (Zone 1), another Knudsen cell loaded with Se pellets (99.98%, Sigma Aldrich) was placed on the second zone of the furnace (Zone 2). At the third zone of the furnace (Zone 3), approximately 1-5 μg of MoO₃ were placed on a SiO₂/Si wafer and the Au foil was placed at the downstream side, next to the wafer. In every growth experiment, together with the Au foils, we have placed a piece of Si wafer with 300 nm thermal oxide layer (Siegert Wafer) to investigate the substrate influence. Next, the quartz tube was evacuated to 1×10^{-2} mbar pressure and refilled with argon (5.0,

Linde). The whole growth process was carried out under an argon flow of 100 cm³/min and ambient pressure. The argon gas flow was used to carry the chalcogen atoms to the high temperature reaction area where the growth substrates (Au foils and SiO₂/Si) were located. A two-step heating protocol was used for subsequent growth of MoSe₂, and conversion of Janus structure as explained step by step below.

Step 1: CVD synthesis of ML MoSe₂ on Au Foils: Initially, the third zone (Zone 3) containing the metal oxides precursor (MoO₃) and the Au foils is heated to the growth temperature of 720 °C at a rate of 40 °C/min and held at that temperature for 10 to 30 minutes. The temperature of the second zone (Zone 2) with selenium (Se) was adjusted to reach ~400 °C when the temperature of the growth zone (Zone 3) reaches 700 °C. At the same time, the first zone (Zone 1) with sulfur (S) precursor remains at room temperature. When the temperature of the third zone reaches 720 °C, we introduced hydrogen (5.0, Linde) at a flow rate of 5 cm³/min. The hydrogen flow was turned off after the growth, and the furnace was cooled down to 500 °C under an argon flow of 100 cm³/min. Then the body of the split furnace was opened to rapidly cool down the sample to room temperature. This procedure results in the growth of ML MoSe₂ on Au surface. Note that the Ar flow was maintained constant during all the steps from the very beginning of the experiment.

Step 2: Conversion of MoSe₂ to Janus SeMoS: After the furnace cooled down to room temperature, the first zone with S precursor and the third zone with Au foils with grown MoSe₂ crystals were reheated to 200 °C and 700 °C, respectively. The samples were exposed to the S vapor for 10 min at this temperature. The middle zone (Zone 2) was maintained at a temperature 100 °C to prevent condensation of S during transport to Zone 3. After the conversion process, the split tube furnace was opened to rapidly cool the sample to room temperature. Note that the Ar flow of 100 cm³/min is maintained constant during all the steps from the very beginning of the experiment until opening the chamber to prevent any possible degradation when in contact with air/or atmospheric moisture. This procedure results in the successful conversion of ML MoSe₂ to ML Janus SeMoS on the Au surface.

Similar one-pot synthesis approaches were also previously reported for the preparation of TMD alloys^[5-7] and lateral heterostructures.^[4]

Electrochemical delamination transfer of Janus SeMoS films from Au foils

After growth, the ML Janus SeMoS were detached from the Au foils and transferred onto SiO₂/Si wafers using an electrochemical delamination^[8,9] transfer method. A PMMA layer of 200 nm (950 kDa, Allresist GmbH, AR-P 679.04) was spin coated onto the Au foil with ML Janus

SeMoS. Then, applying a constant current of 20 mA, the PMMA/ML Janus SeMoS was gradually separated from the Au foil by H₂ microbubbles produced by water electrolysis in a 0.2 M NaOH solution. After that, the PMMA/ML Janus SeMoS was collected by the target SiO₂/Si wafers, followed by a typical acetone and isopropyl alcohol bath process to remove the PMMA support. Using the same electrochemical delamination transfer process, we additionally transferred Janus MLs on SiO₂/Si substrates where high-quality hBN flakes^[10] were exfoliated prior to transfer. A last step included the transfer of a thin, top hBN to encapsulate the Janus MLs for the low-temperature optical spectroscopy experiments.

Basic characterization of the ML Janus SeMoS

Optical microscopy

The optical microscopy images were taken with a Zeiss Axio Imager Z1.m microscope equipped with a thermoelectrically cooled 3-megapixel CCD camera (AxioCam 503 color) in bright field operation.

Atomic force microscopy

The AFM measurements were performed with a Ntegra (NT-MDT) system in tapping mode at ambient conditions using n-doped silicon cantilevers (NSG01, NT-MDT) with resonant frequencies of 87 – 230 kHz and a typical tip radius of < 6 nm.

Raman spectroscopy

The Raman spectra and mapping were acquired using a Bruker Senterra spectrometer operated in backscattering mode. Measurements at 532 nm were obtained with a frequency-doubled Nd:YAG Laser, a 50x objective and a thermoelectrically cooled CCD detector. For all spectra the Si peak at 520.7 cm⁻¹ was used for peak shift calibration of the instrument. The Raman spectroscopy maps were obtained using a motorized XY stage and analyzed by fitting a Lorentzian function to the data using a LabView script.

Angle-resolved X-ray photoelectron spectroscopy (ARXPS)

XPS was performed in an ultra-high vacuum (base pressure 2×10^{-10} mbar) Multiprobe system (Scienta Omicron) using a monochromatized X-ray source (Al K _{α}) and an electron analyzer (Argus CU) with a spectral energy resolution of 0.6 eV. During the ARXPS measurement, the emission angle (θ) was varied from 0° to 80° whereas the source-analyzer angle (54.7°) was fixed. The spectra were calibrated using the Au 4f_{7/2} peak (84.0 eV) or Si 2p peak (SiO₂, 103.5 eV), respectively and fitted using Voigt functions (30:70) [for Au 4f: (20:80)] after a linear (S 2p, Se 3d) or Shirley-background (Mo 3d, Au 4f) subtraction. To perform the quantification, the relative sensitivity factors (RSF, Tab. S3) provided by CasaXPS were used.

Electron microscopy

Janus structures were transferred to epi-ready Si wafers that act as substrate for a cross sectional transmission electron microscopy (TEM) investigation. The TEM lamella for cross sectional TEM investigations were prepared using a focused ion beam (FIB) system of the type Zeiss NVision 040. First, an appropriate sample structure (Fig. S13) was selected and then a protection layer of carbon was deposited using the gas injection system (GIS). The structure was free-cut using a high current 30kV Ga-ion beam. The lamella was transferred to a lift-out TEM-grid (Omniprobe company) and subsequently fine-polished to thickness of about 25 nm using a 5 kV low current Ga-ion beam. Scanning (S) TEM investigations was carried out at 200 kV using a Thermofisher Talos 200X operating at 200 kV. A SuperX detector was used to acquire EDX mappings. Quantification of the EDX data was done using the Thermofisher Velox software package. Aberration corrected HRTEM images of free-standing Janus structures were acquired using the dedicated low voltage SALVE (Sub-Ångström low voltage electron microscopy, <https://www.salve-center.de>) TEM at 80 kV. For the suspended Janus SeMoS crystals were prepared by transferring the as grown crystals onto Quantifoil® grids by a transfer protocol which involves critical point drying as reported previously.^[11]

DFT Calculations

The energetics of the atomic configurations relevant to the exchange mechanism was studied using spin-polarized density functional theory (DFT) as implemented in the VASP code.^[12, 13] All the calculations were carried out using the PBE exchange-correlation functional^[14] and the PAW method.^[15] The van der Waals (vdW) interaction was accounted for using the Grimme scheme.^[16] The structures were fully optimized with an energy cut-off of 400 eV and a force tolerance of 0.01 eVÅ⁻¹. The MoSe₂/Au (111) system was modelled as a periodic 8×8 MoSe₂ by 9×9 Au supercell composed of 324 Au atoms (four closely packed layers) and 64/128 Mo/Se atoms. The supercell size was chosen to match the theoretical values of the unit cell parameters of the materials, giving rise to a strain of less than 1%. A vacuum space of 15 Å in the perpendicular direction was used. The Brillouin zone of the systems was sampled using 2×2×1 Monkhorst-Pack grid. The test calculations with a 4×4×1 grid gave essentially the same results. The nudged elastic band (NEB) method^[17] was employed to access migration barriers. These calculations were performed using the same 9×9 Au supercell and employed a 2×2×1 Monkhorst-Pack grid with an energy cut-off of 400 eV. A set of 7 images were used to evaluate the migration barrier, however, due to the symmetry of the diffusion pathway this increases to an effective 13 images.

Low temperature optical spectroscopy

Two different optical setups were used for the optical spectroscopy experiments.

For the low-temperature PL, Raman, PLE and reflectivity experiments we use a home-built microscope in a liquid helium (LHe) closed-cycle cryostat system (Attocube, Atto700). A HeNe 633 nm laser is used for the PL and Raman experiments, while for the PLE we utilize a supercontinuum white light laser (NKT Photonics) with a tunable high contrast filter that allows selectivity of the excitation wavelengths. A combination of linear polarizers, halfwave and quarter waveplates allowed the control of excitation and detection polarization for the polarization-resolved Raman and circular polarization PL measurements. The light is focused onto the sample using a microscope objective while the temperature of the sample is kept at $T = 5$ K. Cryogenic nanopositioners (nm steps, mm range) are used to control the position of the sample with respect to the laser beam. The back-reflected light from the sample is dispersed in a 500mm monochromator (ACTON SpectraPro 2500i, Princeton Instruments) with a 150 g/mm grating (600g/mm in the Raman experiments). The spectra are recorded by a liquid-nitrogen cooled charged coupled device (CCD) array. Low temperature reflectivity experiments are performed using a tungsten-halogen lamp as a white-light source with a stabilized power supply, focused initially on a pinhole that is imaged on the sample. The excitation/detection spot diameter is $\approx 1\mu\text{m}$, i.e., smaller than the typical diameter of the sample.

Magneto-PL experiments have been carried out in an ultra-stable confocal microscope (Attocube, Atto1000) with cryogenic nanopositioners at $T = 4$ K and in magnetic fields up to 9 T in a Faraday geometry. The detection spot diameter is about 700 nm. The sample is excited by a He-Ne laser (1.96 eV) with linear polarization and both circular σ^+ and σ^- polarized PL signals are detected using a liquid crystal retarder and an analyzer in the detection path. The PL emission is dispersed in a monochromator and detected with a Si-CCD camera.

Supplementary Note 2: Comparison with previous reports on Janus TMD synthesis

In general, the previous reports on the preparation of Janus TMDs rely on the replacement of uppermost chalcogens induced by plasma-assisted treatment^[18-21] (hydrogen or Se plasma). The general idea is to strip away the top atomic layer by plasma and replace with another chalcogen atom. However, this technique needs the use of plasma treatment, which increases the process complexity. Furthermore, the exposure of the starting transition metal dichalcogenide (TMD) crystal to plasma can create additional unwanted defects^[22] in the crystal structure. Although this challenge may be partly mitigated through careful synthetic design to enable the successful growth of Janus TMDs, it highly relies on the precise control of many growth parameters

(sample positioning, plasma power, high-temperature duration time, and many other parameters related to the kinetics of the reaction).^[19-21] In addition, an optimized distance must be maintained between the plasma tail and the growth substrate, leading to short working windows,^[19, 20] thus the controllable growth of large-area Janus TMDs using such a strategy is very challenging. On the other hand, our one-pot CVD approach of growing Janus TMDs on the Au surface is rather straight-forward and easy to reproduce with simple CVD equipment. Another approach reported for the synthesis of Janus TMD is the high temperature (~ 800 °C) sulfurization of CVD ML MoSe₂ grown on SiO₂/Si substrate.^[23] However, such high temperature treatment performed on the CVD grown ML MoSe₂ crystals result in the material degradation in our experience, especially when using TMD crystals grown in a separate CVD process. We provide our experimental results on our attempt on SiO₂/Si in which we used the similar one-pot approach used for the growth of ML Janus SeMoS in Supplementary Note 5.

Supplementary Note 3: Detailed explanation of DFT calculations confirming the growth mechanism

To get a microscopic insight into the mechanism of Janus structure formation, we carried out density-functional theory (DFT) calculations aimed at assessing the energetics of various atomic configurations relevant to the synthesis process. Technical details of calculations are given in method section. The adsorption and migration of S and Se atoms on Au (111) surface were considered, as well as their interaction with the free-standing and supported MoSe₂ monolayer, as schematically illustrated in Figure S5. Our calculations indicate that it is energetically favorable to substitute a Se atom with S atom, but the energy difference is small (about 0.3 eV), consistent with previous theoretical and experimental reports on MoSSe alloys.^[24] Then we studied the atom exchange in the combined MoSe₂/Au system represented by a 8×8 MoSe₂/ 9×9(111)Au supercell, Figure S2. Various positions of the S atom in the moiré pattern were considered. These calculations gave roughly the same results as for the free-standing material (the energy difference was less than 0.1 eV) for all the positions, even when placed in the upper and bottom layer of the structure. The reason for that is a smaller atomic radius of S atom as compared to that of Se (105 vs 120 pm, see also Figure S5B), so that the S atom is ‘hidden’ and does not interact with the Au substrate, giving rise to the same replacement energy for the upper and lower layers of MoSe₂. Thus, the imbalance between the concentration of S atoms in the upper and bottom layers should be governed not by the energetics, but kinetics of the process. To address this conjecture, we considered the adsorption and migration of S and Se atoms on Au surface. The calculations indicated that it is energetically favorable for S₂/S₈

molecules to split upon adsorption (contrary to the adsorption on MoSe₂), Figure S3. Formation of interstitial atoms in the bulk of Au slab was found to be energetically unfavorable, so that the (111) Au surface should be covered with S adatoms. These are highly mobile at the elevated temperatures used in the experiment with low migration barriers (< 0.4 eV) for adatoms (Figure S4) found by NEB calculations. We note here that it costs more than 5 eV to remove a Se atom from the MoSe₂ sheet, and that splitting of S molecules on the sheet is energetically unfavorable, Figure S5. At the same time, the energy penalty for removing a Se atom from the bottom layer of the sheet followed by the immediate adsorption of the atom on Au surface (outside the flake area) is 1.7 eV only. Thus, one can expect that during annealing the Se atoms in the bottom layers will predominantly be replaced with S atoms. The scenario is summarized in Figure S5.

Supplementary Note 4: Influence of sulfurization time on the formation of ML Janus SeMoS

We have performed a series of ML Janus SeMoS growth experiments on Au foils in which we changed the sulfurization time to 3, 5 and 10 minutes at 700 °C. The effect of sulfurization time on the Janus conversion process is probed by Raman spectroscopy (Figure S7). When the sulfurization time is 3 mins, both of MoSe₂ peak ($A'_{1, 240} \text{ cm}^{-1}$) and Janus SeMoS peak ($A^1_{1, 290} \text{ cm}^{-1}$) can be observed in the Raman spectrum, indicated only the bottom Se layer of the ML MoSe₂ is partially replaced by S atoms. Furthermore, the intensity of the Janus SeMoS peak ($A^1_{1, 290} \text{ cm}^{-1}$) increases with longer conversion time; meanwhile, the intensity of the MoSe₂ peak ($A'_{1, 240} \text{ cm}^{-1}$) decreases and vanishes after 5 mins. When the sulfurization time is prolonged to 10 mins, the Janus SeMoS signature $A^1_{1, 290} \text{ cm}^{-1}$ Raman peak at 290 cm^{-1} exhibits a maximized intensity and minimized FWHM, indicating the optimized sulfurization time.

Supplementary Note 5: Growth of millimeter scale ML Janus SeMoS

The Au surface possesses the chemical inertness and negligible solubility of metal and chalcogen atoms,^[8] allowing the growth of large-area Janus monolayer films. Prolonging the initial MoSe₂ growth step to 30 mins resulted in the growth millimeter scale area growth monolayer films on the Au foil (such film areas formed by merging many crystalline grains of MoSe₂). Then it is worth directly extending the conversion process to obtain continuous millimeter scale Janus SeMoS films. The Raman spectroscopy analysis performed on the Janus SeMoS films (Figure S9) shows identical Raman spectra at many different spots with narrow $\text{FWHM} = 4.6 \pm 0.2 \text{ cm}^{-1}$ indicating uniformity and high crystalline quality of the Janus SeMoS films.^[18, 20, 23]

Supplementary Note 6: Growth attempt of ML Janus SeMoS on SiO₂/Si

We performed all the growth and sulfurization processes on SiO₂/Si substrate together with the Au foils for direct comparison between the growth on Au foils and SiO₂/Si substrates at different temperatures. The Raman spectroscopy data performed on the grown material on SiO₂/Si substrate is provided in Figure S10. As evident from the Raman spectra we could only observe the formation of MoS₂(1-x)Se_{2x} alloy^[25] and Janus SeMoS did not occur. The samples sulfurized at 850 °C show characteristics peaks of MoS₂ with broader full width at half maximum (FWHM) indicating the conversion to highly defective MoS₂.^[26, 27] In addition, when the sulfurization temperature is below 700 °C, only the MoSe₂ signature can be observed, which indicates that S does neither substitute the top and nor bottom Se layer of ML MoSe₂ without the catalytic effect of the Au substrate.

Supplementary Note 7: Angle-resolved X-ray photoelectron spectroscopy

For the as grown Janus SeMoS sample the main peaks are already discussed in main the paper. From quantification of the SeMoS components in the Mo 3d, S 2p and Se 3d regions we calculate the ratios of Se:Mo:S to be 0.9(2):1.0(2):1.5(2) indicating a S excess. This excess could be explained by S-Au or C-S-Au bounds, which are located at a binding energies (BE) of ≈ 161.3 eV^[28] and ≈ 161.9 eV (S 2p_{3/2}),^[29] respectively. Thus, it isn't possible with XPS to distinguish S atoms which are bound to the substrate or arranged in the Janus SeMoS structure.

For calculation of the relative intensity (RI) according to the equation $RI = \frac{I(x, \theta) / I(x, 0^\circ)}{I(Au, \theta) / I(Au, 0^\circ)}$ the intensities of the SeMoS peaks in the Mo 3d, S 2p and Se 3d region as well as the Au 4f substrate peaks (Figure S11) for different emission angles θ are included. The RI values show the θ -dependend intensity change of each element $I(x, \theta) / I(x, 0^\circ)$ ($x = \text{Se, Mo, S and Au}$) relative to the change of intensity of the substrate peaks $I(Au, \theta) / I(Au, 0^\circ)$. If we take the fact into account that the higher θ the higher the surface sensitivity and the lower the information depth $d = \lambda \cos \theta$ where λ is the attenuation length,^[30] we can directly derive the relative positions of Se-, Mo- and S-atoms in a quantitative manner from Figure 2B. The highest RI values we obtain for Se followed by Mo and S. Thus, we find from ARXPS measurements that Se is the top layer and S the bottom layer. This result confirms the exchange of the bottom Se layer in MoSe₂ with S atoms as described in the main paper. In addition, we could observe further components marked in Figure 2A. In the Mo 3d region we see a doublet at ≈ 231.0 eV (Mo 3d_{5/2}) and ≈ 234.2 (Mo 3d_{3/2}) originating from the precursor MoO_x. Also, the S 2s (BE = 226.2(1) eV) and

Se 3s (BE = 229.3(2) eV) orbitals are overlapping with this spectrum. Besides the sharp S 2p doublet already discussed, there is a second S doublet observed at higher binding energies (BE[S 2p_{3/2}] = 163.6(2) eV). These photoelectrons originating from S which is probably arranged in S₂ or S₈ molecules on the surface. This second S doublet was not considered for the calculation of RI, as well as the MoO_x in the Mo 3d spectra. In the S 2p region also the Se 3p orbital is overlapping. We can separate these peaks from S 2p peaks due to the larger full width of half maximum (FWHM) and larger spin-orbit splitting.^[31] The intensity ratio between Se 3p and S 2p increases for higher emission angle clearly shown in Figure 2A. Thereby, we can directly see that Se must be higher-lying than S. In the Se 3d region the Se 3d doublet originating from the Janus SeMoS structure is overlapping with the Au 5p_{3/2} substrate peak as well as the Mo 4s orbital. Information about the components discussed are summarized in Tab. S1. Further elements on the samples are O and C (Figure S11) originating mostly from the ambient conditions (or from MoO_x). For the transferred Janus SeMoS to SiO₂/Si similar SeMoS peaks for each element could be observed (Figure S12). Whereby, the intensity ratios of Se:Mo:S are calculated to be 0.8(2):1.0(2):1.3(2) which roughly fits the expected structure of 1:1:1. The measured S excess for samples on gold is reduced here because the S bond to the Au substrate is not transferred and just the S in the Janus SeMoS configuration contribute to the main S peaks. Besides this behavior, also the S 2p peaks originating from the S₂ or S₈ molecules disappear. Information about the peaks for the Janus SeMoS on SiO₂/Si are given in Tab. S2. Note, the discussed transferred Janus SeMoS was a different sample compared to the discussed Janus SeMoS on Au foil.

Table S1: Quantitative analysis of the high-resolution XP spectra shown in Figure 2A of the main paper including the peak assignment, their binding energies, their full width at half maximum (FWHM) and areas obtained from the spectra deconvolution. For the p and d photoelectron doublets, the fixed intensity ratios of 2:1 as well as 3:2 originating from spin-orbit coupling are used except for the Se 3d orbital. Here, an intensity ratio of 1.3:1 is employed.^[32] The numbers in the parentheses are the experimental error represented as the uncertainty of the last digit.

Peak Assignment	Binding energy, eV	FWHM, eV	Area, %
Janus SeMoS on Au foil			
$\theta = 0^\circ$			
$\theta = 75^\circ$			
Mo 3d_{5/2} (SeMoS)	228.7(1)	0.7(1)	48(2)
	228.8(1)	0.7(1)	46(2)
Mo 3d_{3/2} (SeMoS)	231.9(1)	0.9(1)	32(2)
	231.9(1)	1.0(1)	31(2)
Mo 3d_{5/2} (MoO_x)	231.0(3)	3.0(3)	12(2)
	231.3(3)	3.0(3)	14(2)
Mo 3d_{3/2} (MoO_x)	234.2(3)	3.0(3)	8(2)
	234.4(3)	3.0(3)	9(2)
Se 3s	229.2(3)	1.9(2)	100
	229.6(3)	2.6(2)	100
S 2s	226.2(2)	2.1(2)	100
	226.3(2)	2.6(2)	100
S 2p_{3/2} (SeMoS)	161.6(1)	0.9(1)	57(2)
	161.7(1)	0.8(1)	54(2)
S 2p_{1/2} (SeMoS)	162.8(1)	0.9(1)	28(2)
	162.9(1)	0.8(1)	27(2)
S 2p_{3/2} (S₂, S₈)	163.7(2)	1.2(2)	10(2)
	163.8(2)	1.1(2)	13(2)
S 2p_{1/2} (S₂, S₈)	164.9(2)	1.2(2)	5(2)
	165.0(2)	1.1(2)	7(2)
Se 3p_{3/2}	160.5(1)	1.6(1)	67
	160.6(1)	1.6(1)	67
Se 3p_{1/2}	166.3(1)	1.6(1)	33
	166.4(1)	1.6(1)	33
Se 3d_{5/2} (SeMoS)	54.2(1)	0.7(1)	58
	54.2(1)	0.7(1)	58
Se 3d_{3/2} (SeMoS)	55.0(1)	0.7(1)	42
	55.0(1)	0.7(1)	42
Au 5p_{3/2}	57.1(2)	5.1(3)	100
	57.2(2)	4.3(3)	100
Mo 4s	62.7(2)	4.4(2)	100
	62.9(2)	3.5(2)	100

Table S2: Quantitative analysis of the high-resolution XP spectra including the peak assignment, their binding energies, their FWHM and areas obtained from the spectra deconvolution. For the p and d photoelectron doublets, the fixed intensity ratios of 2:1 as well as 3:2 originating from spin-orbit coupling are used except for the Se 3d orbital. Here, an intensity ratio of 1.3:1 is employed.^[32] The numbers in the parentheses are the experimental error represented as the uncertainty of the last digit.

Peak Assignment	Binding energy, eV	FWHM, eV	Area, %
Janus SeMoS on SiO₂/Si			
$\theta = 0^\circ$			
$\theta = 75^\circ$			
Mo 3d_{5/2} (SeMoS)	229.0(1)	0.9(1)	53(2)
	228.9(1)	1.0(1)	53(2)
Mo 3d_{3/2} (SeMoS)	232.2(1)	1.0(1)	36(2)
	232.1(1)	1.2(1)	36(2)
Mo 3d_{5/2} (MoO_x)	232.0(3)	3.0(3)	7(2)
	231.5(3)	2.0(3)	7(2)
Mo 3d_{3/2} (MoO_x)	235.1(3)	3.0(3)	4(2)
	234.6(3)	2.0(3)	4(2)
Se 3s	229.3(3)	2.7(2)	100
	228.9(3)	3.0(2)	100
S 2s	226.4(2)	1.9(2)	100
	226.2(2)	1.6(2)	100
S 2p_{3/2} (SeMoS)	161.9(1)	0.8(1)	67
	161.8(1)	0.9(1)	67
S 2p_{1/2} (SeMoS)	163.1(1)	0.8(1)	33
	163.1(1)	0.9(1)	33
Se 3p_{3/2}	160.7(1)	1.6(1)	67
	160.6(1)	1.8(1)	67
Se 3p_{1/2}	166.5(1)	1.6(1)	33
	166.4(1)	1.8(1)	33
Se 3d_{5/2} (SeMoS)	54.4(1)	0.8(1)	58
	54.3(1)	1.0(1)	58
Se 3d_{3/2} (SeMoS)	55.2(1)	0.8(1)	42
	55.1(1)	1.0(1)	42
Se loss	59.2(3)	3.7(3)	-
	-	-	-
Mo 4s	63.6(2)	2.7(2)	100
	63.4(2)	2.0(2)	100

Table S3: Quantitative analysis of the SeMoS components of the high-resolution Mo 3d, S 2p and Se 3d XP spectra for different emission angles θ . For quantification the relative sensitivity factors (RSF) from CasaXPS depending on the orbital, the analyser and the set-up geometry are used to be able to compare the peak intensities for different elements. These RSF values for Mo 3d_{5/2}, S 2p_{3/2} and Se 3d_{5/2} are 5.62, 1.11 and 1.36, respectively. The numbers in the parentheses are the experimental error represented as the uncertainty of the last digit.

Emission angle θ	Mo (SeMoS), at%	S (SeMoS), at%	Se (SeMoS), at%
Janus SeMoS on Au foil			
0°	28(2)	45(2)	27(2)
20°	29(2)	43(2)	28(2)
40°	28(2)	45(2)	27(2)
60°	29(2)	40(2)	31(2)
70°	30(2)	36(2)	34(2)
75°	30(2)	35(2)	35(2)
80°	29(2)	36(2)	35(2)
Janus SeMoS on SiO₂/Si			
0°	32(2)	43(2)	24(2)
75°	32(2)	38(2)	30(2)

Supplementary information Note 8: Magneto-optical measurements

We perform magneto-optics measurements^[33] in a static magnetic field of $B = 9$ Tesla applied perpendicular to the monolayer (Faraday geometry) in our hBN encapsulated samples. In this perpendicular magnetic field, the degeneracy of the optical transitions in the K^+ and K^- valley is lifted as they are energetically separated by the valley Zeeman splitting $\Delta Z = \mu_B g_X B$. In the detection path we use a liquid crystal retarder, that allows to gradually change optical retardation from zero to multiples of the emission wavelength ($0, \frac{\lambda}{4}, \frac{\lambda}{2}, \dots$). As a function of the applied voltage the detected PL is therefore first linear, then elliptical, then circular and then linear again, as sketched in Figure 3E. The sample is excited with linearly polarized light.

Optical spectroscopy analysis

In Figure 3C we plot the emission energy of the X peak as a function of temperature. We fit the characteristic redshift of the bandgap with an empirical formula that allows us to extract an average phonon energy $\langle \hbar\omega \rangle$:

$$E_G^T = E_G(0) - S\langle \hbar\omega \rangle \left\{ \coth \left[\frac{\langle \hbar\omega \rangle}{2k_B T} \right] - 1 \right\}$$

here, $E_G(0)$ is the optical gap at $T = 0$ K, S is a dimensionless coupling constant, k_B is Boltzmann's constant and $\langle \hbar\omega \rangle$ is the average phonon energy. We obtain values of $E_G(0) = (1.778 \pm 0.001)$ eV, $S = 2.4 \pm 0.1$ eV and $\langle \hbar\omega \rangle = (38.9 \pm 0.7)$ meV, in order of magnitude agreement with reported values on Janus monolayers.^[34] Our CVD grown samples allow access to excitonic properties so far mainly reported for Janus samples from transformed exfoliated flakes.^[34, 35]

In Figure 4A we show power dependent PL measurements using a HeNe laser ($\lambda = 633$ nm), we plot in Figure 4B the integrated PL intensity I_{PL} for the L and the X peak as a function of laser power P that we fit with $I_{PL}(P) = \eta P^b$ where η is a proportionality factor that depends on generation, emission and detection efficiency of the experiment.^[23] The L peak shows a slope below one with $b_L = 0.65$. This indicates saturation of I_{PL} with increasing power due to the finite number of available defect/localization sites. The X peak intensity increases linearly with power as $b_X = 0.97$, which is the signature of a free exciton peak.^[36]

The exciton polarization dynamics in TMD monolayers is governed by the long-range Coulomb exchange interaction.^[37] Although it is challenging to analyse the polarization dynamics from time-integrated measurements in detail, one possibility is that the increased exciton scattering rate at higher temperature leads to a shortening of the exciton polarization lifetime,^[37] and at the same time the PL emission time increases. This would lead to a lowering of the measured

P_c . In addition, in our experiment the laser energy is fixed at 1.96 eV, and the X peak energy strongly decreases with temperature. This change in energy difference for the non-resonant excitation can induce changes in the valley polarization generation and relaxation.

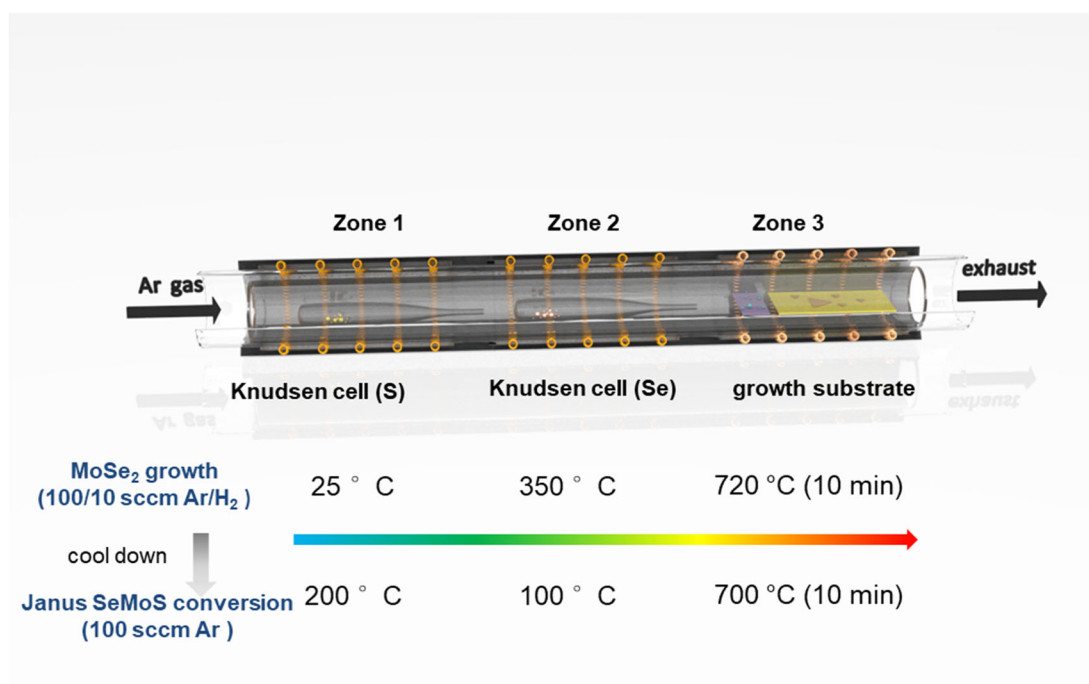


Figure S1: Schematic diagram of the schematic of the one-pot CVD setup with process flow.

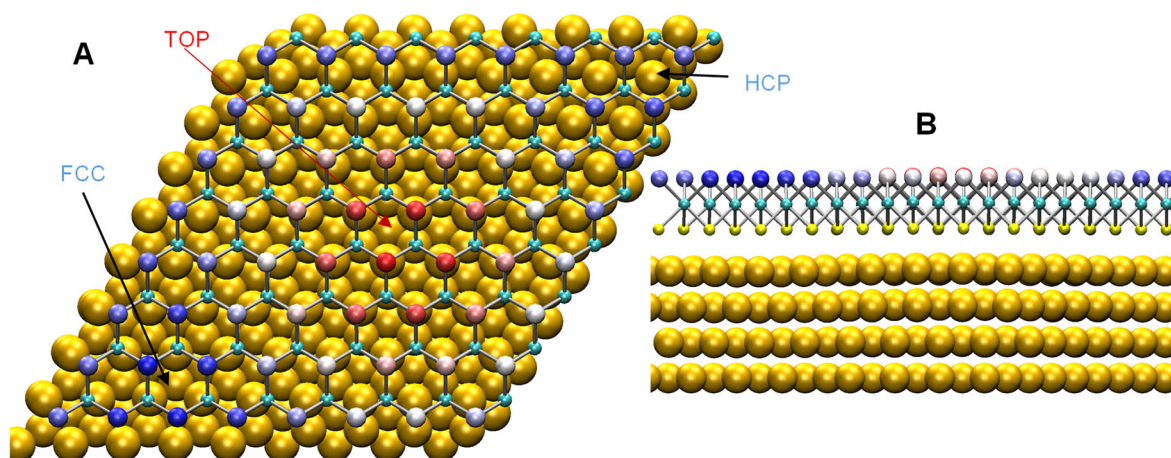


Figure S2: (A) The atomic structure of MoSe₂ sheet on Au(111) surface corresponding to a periodic 8×8 MoSe₂ by 9×9 Au pattern. The top Se atoms are colored according to their elevation, as also seen from panel (B). It is evident that the bottom Se atoms have different atomic environment, e.g., there is an Au atom exactly under Se atom in the TOP area, while no atom under Se atoms in FCC or HCP regions.

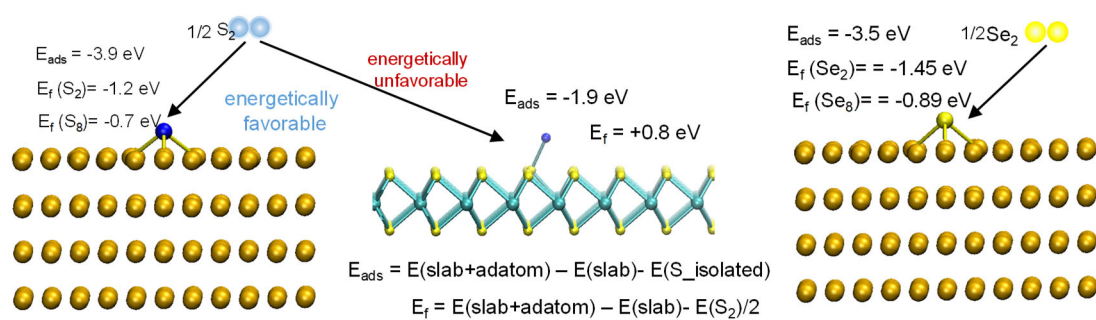


Figure S3: Energetics of S and Se atoms on top of Au (111) and MoSe₂. Adsorption energy E_{ads} is the energy gain upon adsorption of isolated atom, and formation energy of adatom E_f is defined as the energy (per atom) required to break up the S/Se molecule and place the atom on the Au surface or on top of a MoSe₂ sheet.

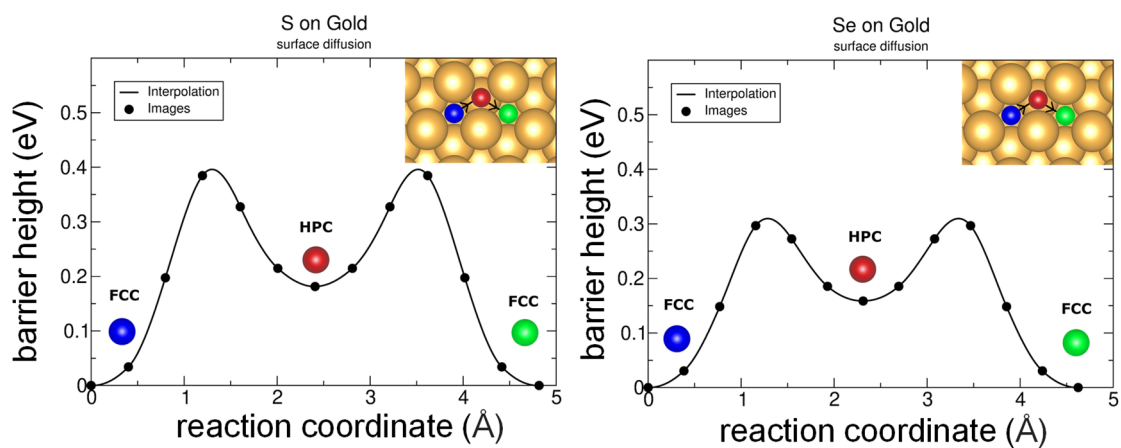


Figure S4: Migration barriers and migration paths of S and Se adatoms on top of Au(111) Au surface as calculated using the NEB method

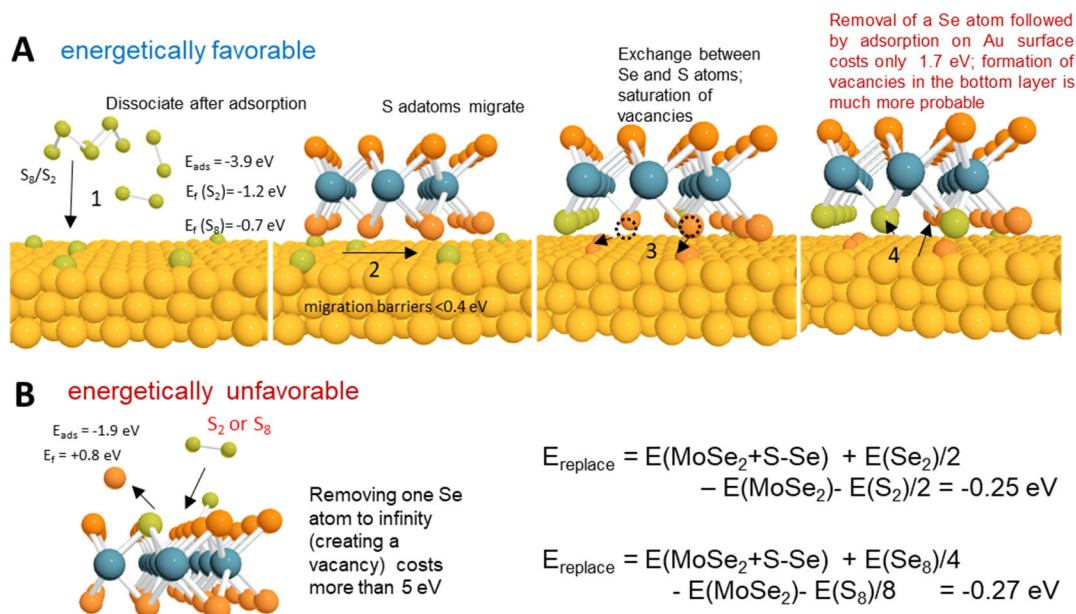


Figure S5: Detailed schematic diagram explaining the conversion mechanism based on replacing bottom Se atoms facing the Au(111) surface with S atoms in S atmosphere as revealed by DFT calculations. **(A)** On Au(111) surface, the S_2 dimers can easily dissociate into S adatoms, which can diffuse very easily at the elevated temperatures used in the experiment because of their low migration energy barriers (< 0.4 eV). In addition, removing a Se atom followed by its adsorption on Au surface requires only 1.7 eV, which is much lower than the energy required (> 5 eV) for direct formation of Se vacancy in MoSe_2 (taking the energy of an isolated Se atom as a reference). At the same time, dissociation of the S_2 dimer on top of MoSe_2 monolayer is energetically unfavorable, as illustrated in panel **(B)**. The replacement of Se atom with S is energetically favorable both in the free-standing and supported MoSe_2 sheet, but the energy gain is roughly the same for both systems. Moreover, the energy only weakly depends on the side and position of the atom in the Moiré pattern. The reason for that is a smaller atomic radius of S atom as compared to that of Se (105 vs 120 pm), so that the S atom is ‘hidden’ and does not interact with the Au substrate, giving rise to the same replacement energy for the upper and lower layers of MoSe_2 . Thus, the imbalance between the concentration of S atoms in the upper and bottom layers should be governed not by the energetics, but kinetics of the process.

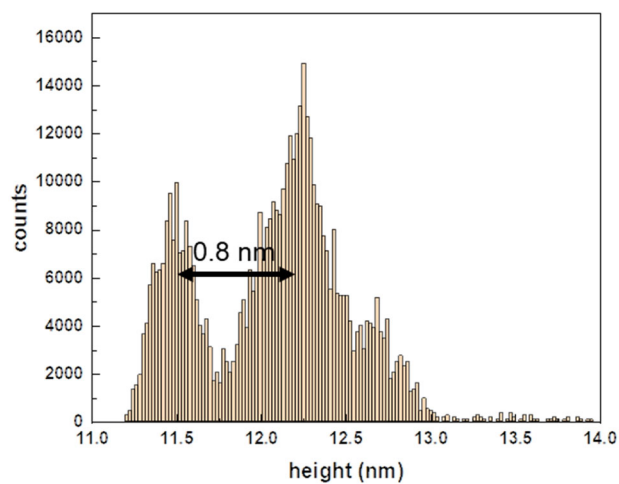


Figure S6: Height distribution histogram between the SiO₂ substrate and a monolayer Janus SeMoS crystal (data extracted from Figure 1D).

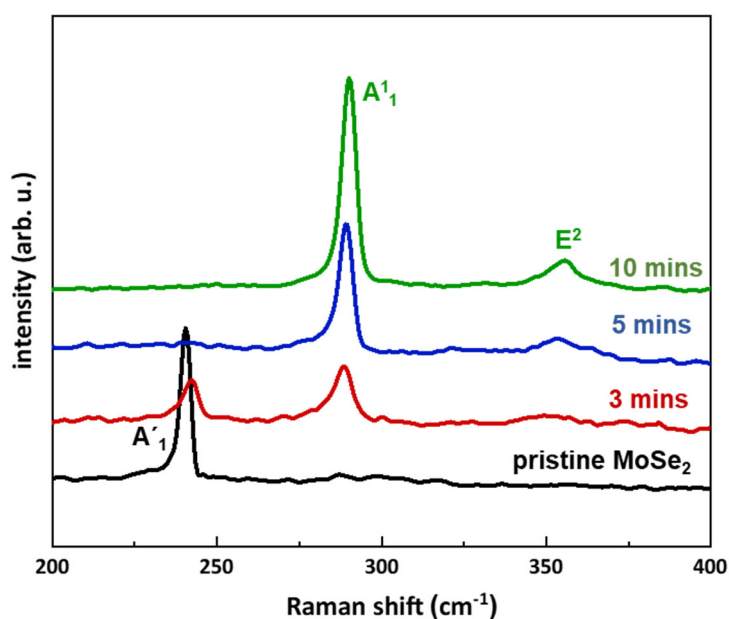


Figure S7: Influence of sulfurization time in the conversion of the monolayer MoSe₂ grown on Au foils to Janus SeMoS. In these experiments different set of monolayer MoSe₂ crystals grown on Au foils were exposed to S vapor at 700 °C for 3, 5 and 10 minutes. The effect of sulfurization time on the Janus conversion process is then probed by Raman spectroscopy. When the sulfurization time is 3 mins, both of MoSe₂ signature (A'_1 , 240 cm^{-1}) and Janus SeMoS signature (A^1_1 , 290 cm^{-1}) can be observed in the Raman spectrum, indicated only partial regions are replaced by S atoms in the bottom Se layer of MoSe₂. Furthermore, the intensity of the Janus SeMoS signature (A^1_1 , 290 cm^{-1}) increases with longer conversion time; meanwhile, the intensity of the MoSe₂ signature (A'_1 , 240 cm^{-1}) decreases and vanishes in 5 mins. While the sulfurization time prolong to 10 mins, the Janus SeMoS signature A^1_1 Raman peak at 290 cm^{-1} exhibits a maximized intensity and minimized FWHM, indicted the optimized sulfurization duration.

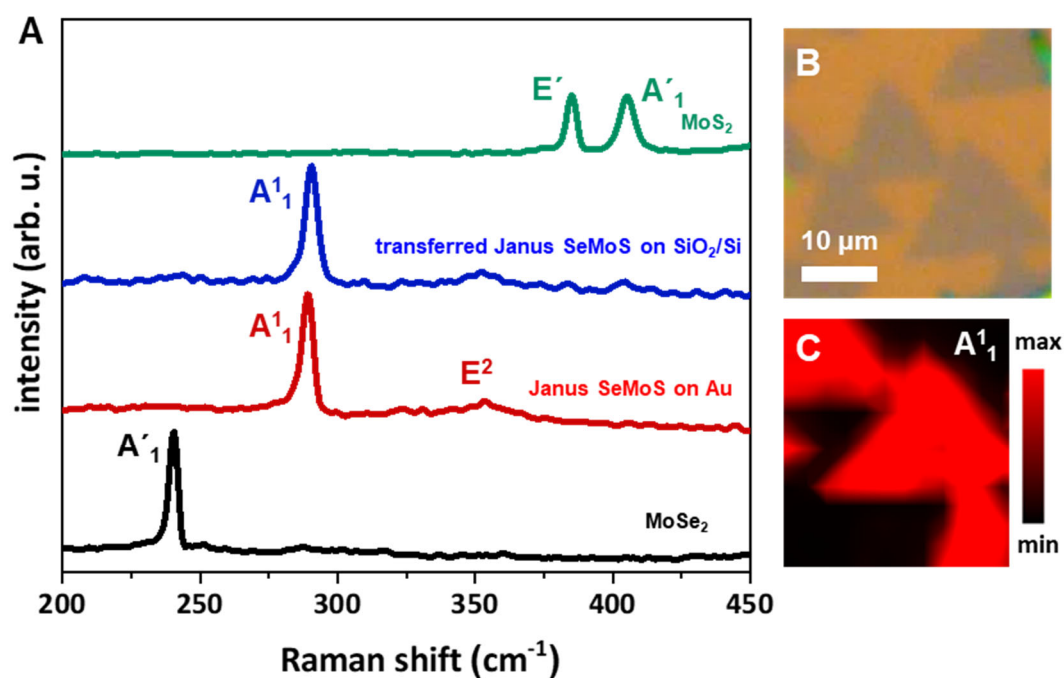


Figure S8: (A) Raman spectra of pristine MoSe₂ on Au, pristine Janus SeMoS on Au, transferred SeMoS on SiO₂/Si on Au and pristine MoS₂ on Au. The as grown and transferred Janus SeMoS monolayer crystals show similar Raman spectra resulting from the successful transfer process without changing the crystal quality. (B) Optical microscopy image (OM) of transferred isolated Janus SeMoS monolayer crystals on SiO₂/Si. The synthesis of isolated Janus SeMoS crystals starts with the growth of MoSe₂ on the Au foil at $\sim 720^\circ\text{C}$ for $\sim 10\text{min}$. (C) Raman intensity mapping performed from (B). The A'₁ mode, originating from the out-of-plane vibration of S-Mo-Se bonds is mapped.

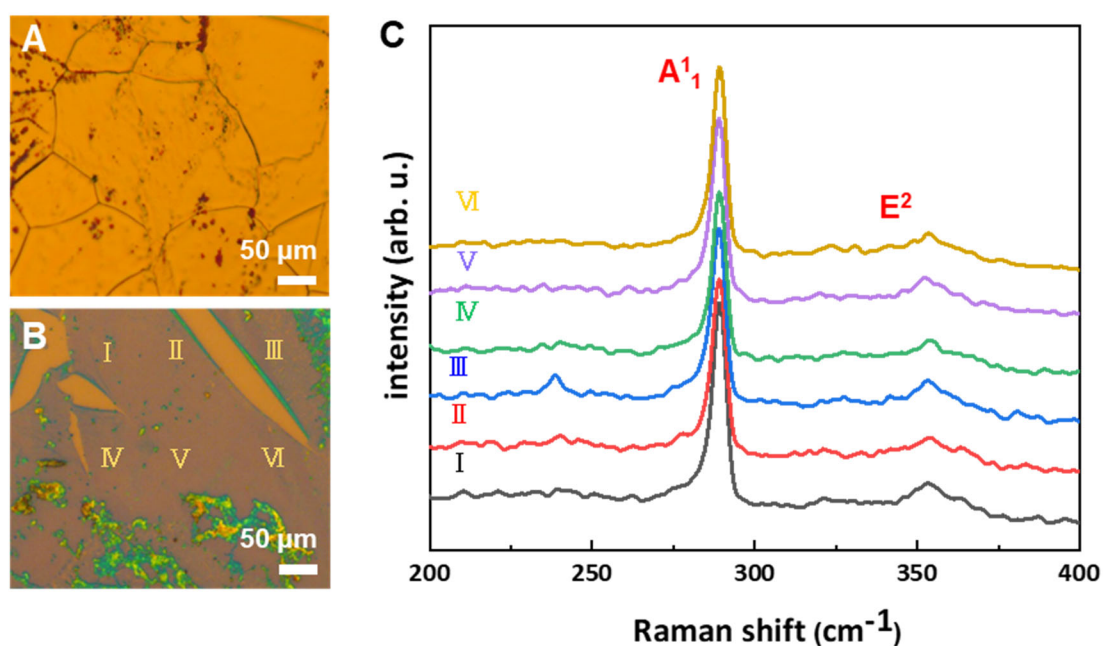


Figure S9: (A) Optical microscopy image (OM) of large-area Janus SeMoS continuous monolayer film on Au foil. The synthesis of Janus film starts with the growth of MoSe₂ continuous film on the Au foil at ~ 720 °C for ~ 30 min. (B) OM of transferred sub-millimeter size Janus SeMoS films. (C) Raman spectra extracted from six different positions over the sub-millimeter sized region in (B). The statistical study shows the uniformity of the large-area Janus SeMoS monolayer film. The narrow FWHM ($\text{FWHM} \approx 4.6 \pm 0.2 \text{ cm}^{-1}$) assessed from these uniform spectra show the high quality of the Janus SeMoS films without the presence of alloying or amorphous regions on the film.

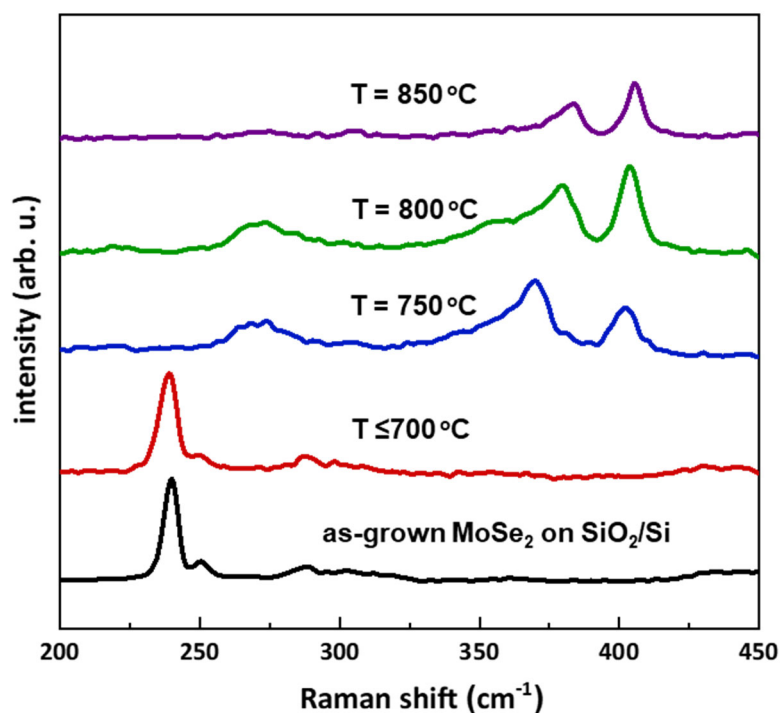


Figure S10: Influence of temperature in the sulfurization process of MoSe₂ ML on SiO₂/Si. Raman spectra showing the influence of temperature in the sulfurization process of MoSe₂ ML on SiO₂/Si. All the growth and sulfurization processes performed together with the Au foils used for data presented in Figure 1E for direct comparison between the growth on Au foils and SiO₂/Si substrates at different temperatures. Monolayer MoSe₂ crystals were first grown on both Au foils and SiO₂/Si substrates in each experiment followed by sulfurization for 10 minutes at different temperatures. Very importantly, no Janus SeMoS Raman signature observed on the crystals grown and sulfurized on SiO₂/Si substrate, while Janus SeMoS Raman signature is observed on the crystals grown and sulfurized on Au foils at 700 °C (for example Figure S8). Furthermore, broader and weak Raman signature can be observed around 270 cm⁻¹ for sulfurization temperatures between 750 °C to 800 °C, corresponding to the formation of (MoS₂(1-x)Se_{2x} alloy).^[38] The samples sulfurized at 850 °C shows characteristics peaks of MoS₂ with broader full width at half maximum (FWHM) indicating the conversion to highly defective MoS₂.^[26, 27] When the sulfurization temperature below 700 °C, only MoSe₂ signature can be observed, which indicated that S does not substitute both of top and bottom Se layer of MoSe₂ monolayer without the catalytic effect of Au substrate. Thus, Au play an essential role during the Janus SeMoS structure formation and can act as catalyst to replace the bottom Se layer.

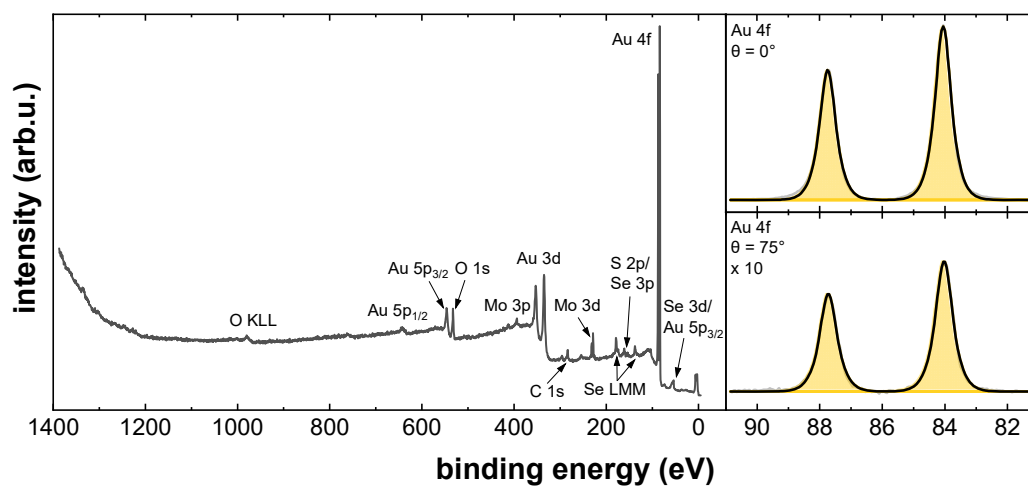


Figure S11: (left) Survey XP spectrum taken at the emission angle with maximum intensity, where the main photoelectron orbital and Auger peaks are named. Besides Se, Mo, S and Au as substrate, C and O could also be measured as adsorbates from the ambient conditions. (right) Au 4f XP spectra at normal emission ($\theta = 0^\circ$, top) and at $\theta = 75^\circ$ (right). The intensity of the spectrum at 75° were multiplied by the 10. These Au peaks are also used for the calculation in Figure 2B.

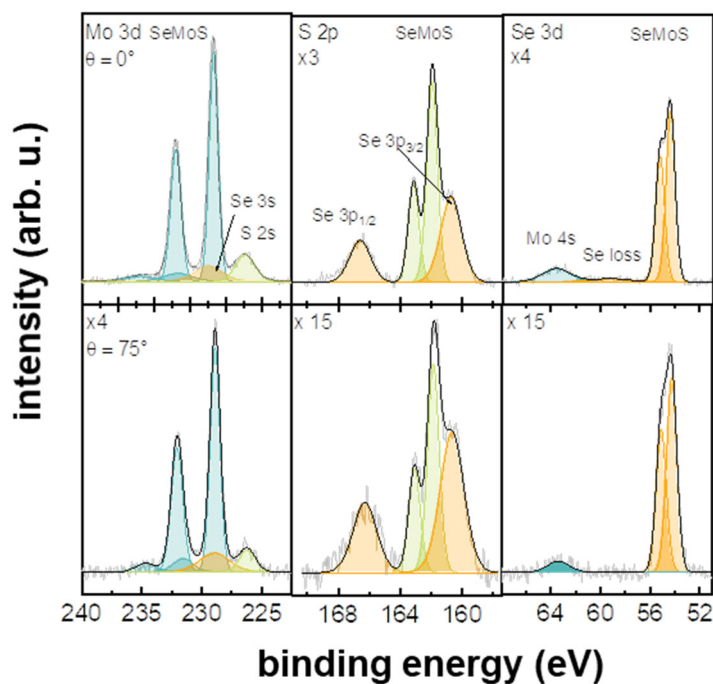


Figure S12: High-resolution Mo 3d, S 2p, and Se 3d XP spectra of transferred Janus SeMoS on SiO₂/Si substrate measured at an emission angle (θ) of 0° (normal emission, top) and 75° (bottom), respectively. After transfer, we see the same SeMoS components in the spectra, which is an indication for a successful transfer. Also, we have the same conclusion, that Se layer should be on top, followed by Mo and S (same procedure as in Figure 2 for calculation, but as substrate we used Si instead of Au). From the S 2p region we directly see this behavior for Se and S, because the Se 3p orbital increases in intensity compared to the S 2p orbital for higher emission angle. In contrast to the as grown Janus SeMoS sample, the sulfur amount is reduced. The ratios Se:Mo:S are calculated to be $0.8 \pm 0.2 : 1.0 \pm 0.2 : 1.3 \pm 0.2$.

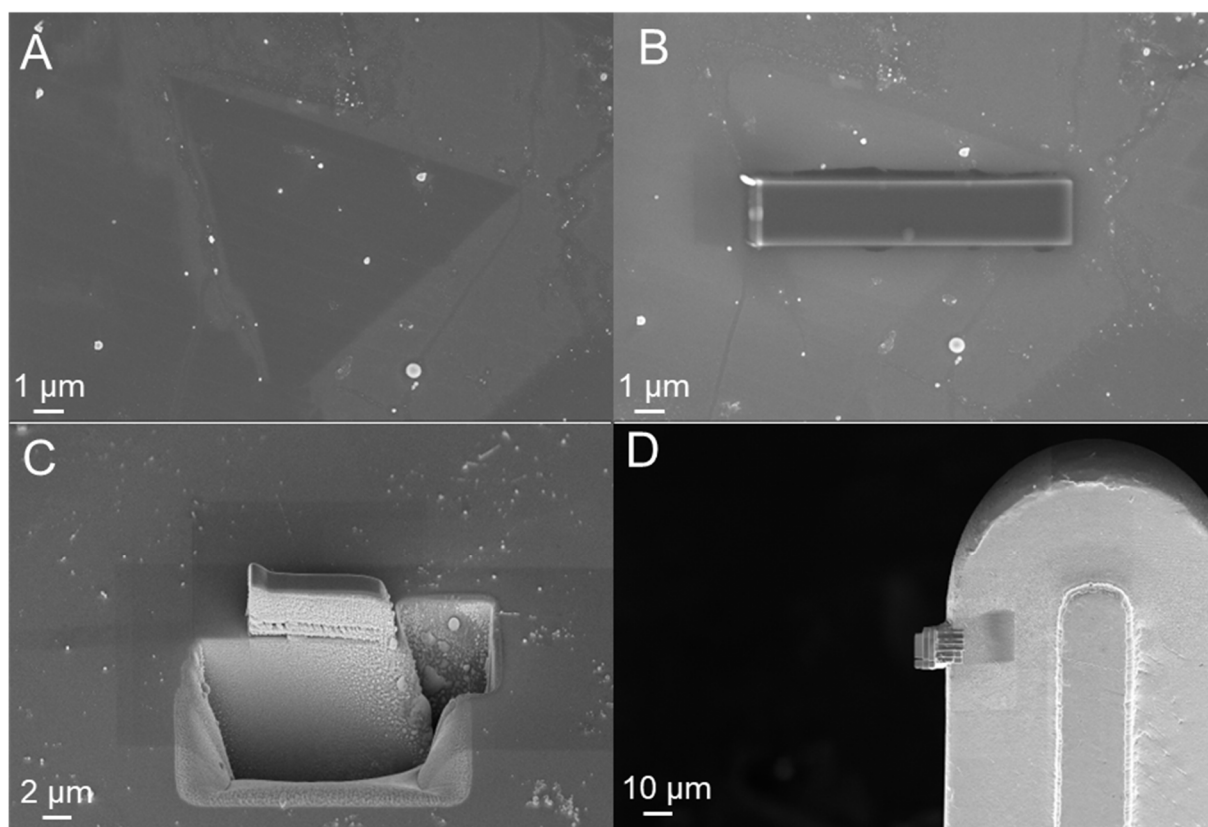


Figure S13: Preparation of the TEM lamella.

- A) Scanning electron microscope (SEM) (inlens detector) image of the selected triangular Janus structure.
- B) SEM image of the triangle after deposition of a carbon protection layer using the GIS (gas injection system). The layer was grown first by using the electron beam deposition to avoid damage of the structure, then, the more efficient Ga-beam deposition was applied.
- C) SEM image after the first Ga-beam cut.
- D) SEM image of the final polished lamella (thinnest area 25 nm) attached to FIB liftout TEM-grid (Omniprobe company).

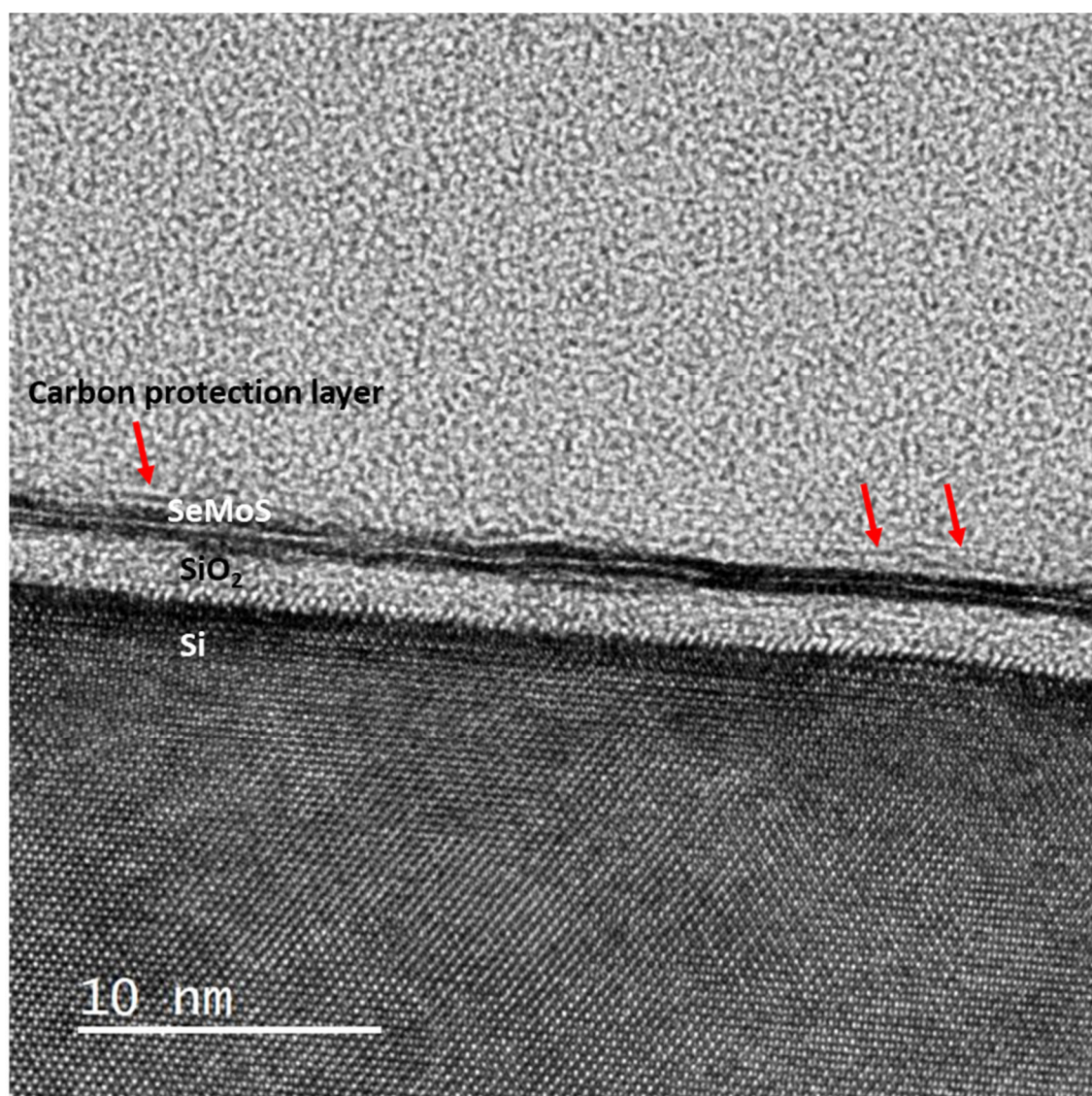


Figure S14: Cross section HRTEM image of the Janus structure on the SiO₂/Si substrate. The three layers of the TMD are visible. Because of the phase contrast mechanism, all three layers appear in similar contrast and the different elements cannot be differentiated. On top of the TMD, leftovers from the sample transfer are visible as graphene-like adsorbates (red arrows).

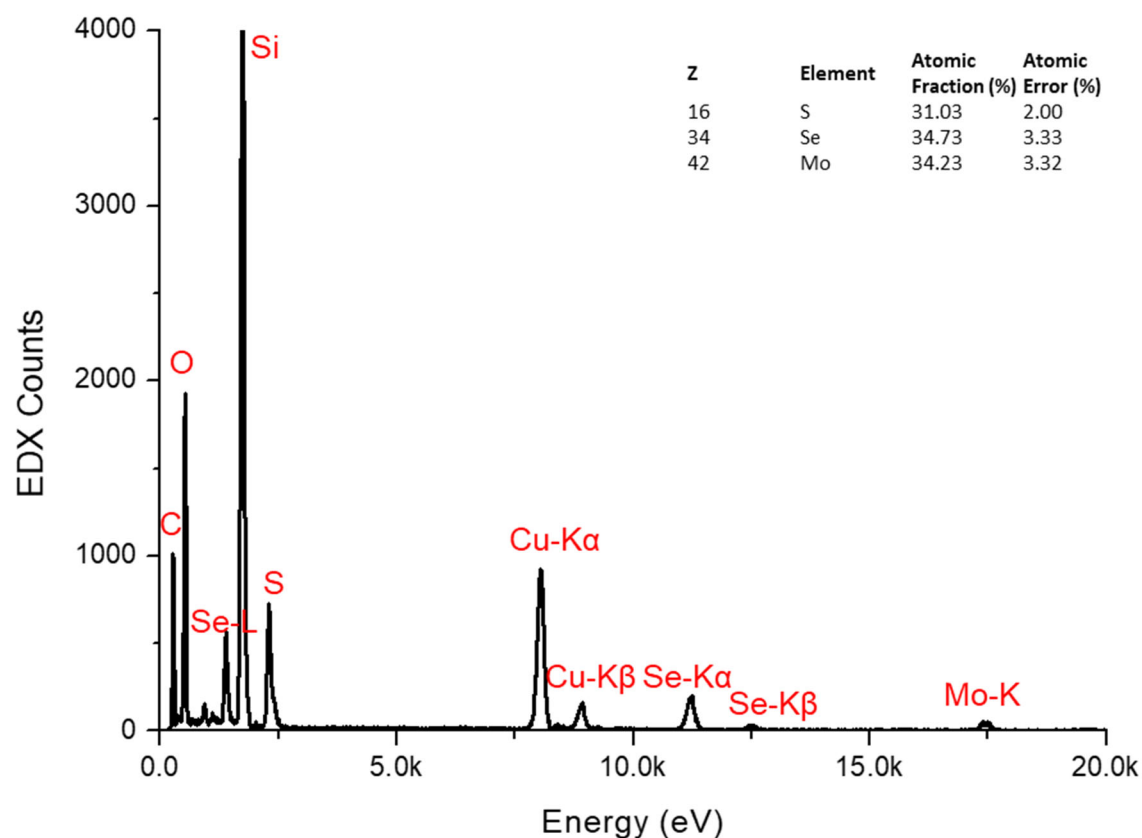


Figure S15: Integrated EDX spectra of the Janus area region (corresponding to Fig. 3D). Besides the elements S, Mo, Se (TMD) also C (protection layer of FIB lamella), Si and O (Si substrate including native SiO₂ layer), and Cu signals (background signal of TEM grid) are detected. The quantification of atomic amount of S, Mo and Se (insert of table) within the TMD results in a ratio of close to 1:1:1 confirming the stoichiometry of Janus SeMoS.

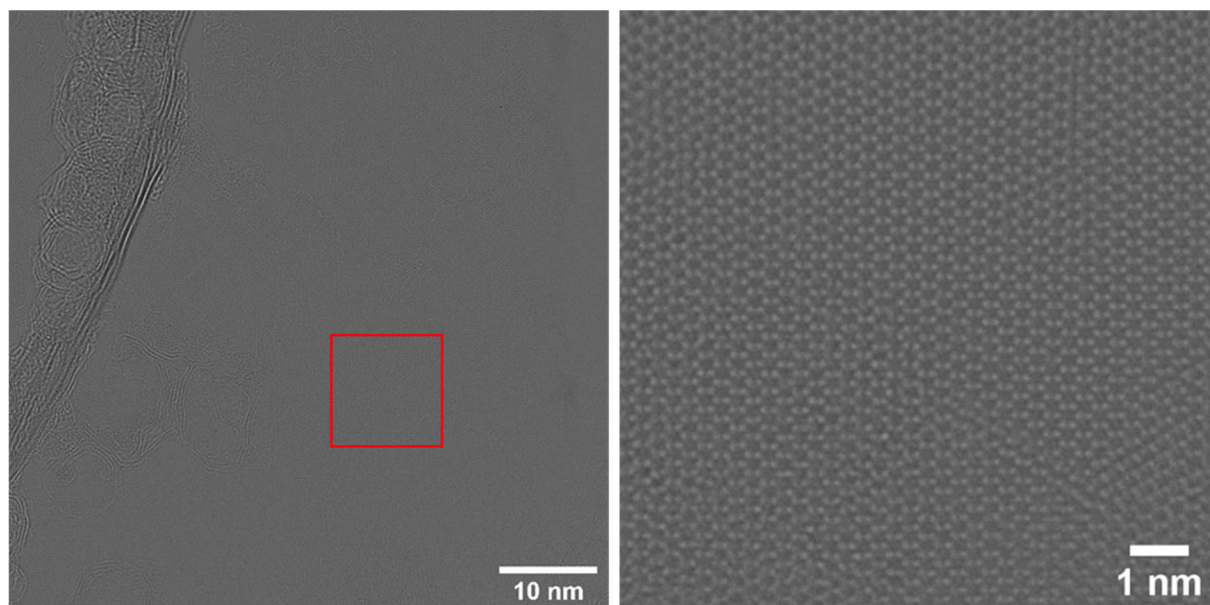


Figure S16: Plane view TEM images of the free-standing Janus structure. (left) Overview image. (right) HRTEM image of the magnified area. The atomic resolved area shows the typical honey-comb structure of a TMD.

References

- [1] S. H. Choi, H.-J. Kim, B. Song, Y. I. Kim, G. Han, H. T. T. Nguyen, H. Ko, S. Boandoh, J. H. Choi, C. S. Oh, H. J. Cho, J. W. Jin, Y. S. Won, B. H. Lee, S. J. Yun, B. G. Shin, H. Y. Jeong, Y.-M. Kim, Y.-K. Han, Y. H. Lee, S. M. Kim, K. K. Kim, Epitaxial single-crystal growth of transition metal dichalcogenide monolayers via the atomic sawtooth Au surface. *Adv. Mater.* **2021**, 33, 2006601.
[10.1002/adma.202006601](https://doi.org/10.1002/adma.202006601)
- [2] P. Yang, S. Zhang, S. Pan, B. Tang, Y. Liang, X. Zhao, Z. Zhang, J. Shi, Y. Huan, Y. Shi, S. J. Pennycook, Z. Ren, G. Zhang, Q. Chen, X. Zou, Z. Liu, Y. Zhang, Epitaxial growth of centimeter-scale single-crystal MoS₂ monolayer on Au(111). *ACS Nano* **2020**, 14, 5036-5045.
[10.1021/acsnano.0c01478](https://doi.org/10.1021/acsnano.0c01478)
- [3] A. George, C. Neumann, D. Kaiser, R. Mupparapu, T. Lehnert, U. Hübner, Z. Tang, A. Winter, U. Kaiser, I. Staude, A. Turchanin, Controlled growth of transition metal dichalcogenide monolayers using Knudsen-type effusion cells for the precursors. *J. Phys. Mater.* **2019**, 2, 016001
[10.1088/2515-7639/aaf982](https://doi.org/10.1088/2515-7639/aaf982)
- [4] E. Najafidehaghani, Z. Gan, A. George, T. Lehnert, G. Q. Ngo, C. Neumann, T. Bucher, I. Staude, D. Kaiser, T. Vogl, U. Hübner, U. Kaiser, F. Eilenberger, A. Turchanin, 1D p-n Junction Electronic and Optoelectronic Devices from Transition Metal Dichalcogenide Lateral Heterostructures Grown by One-Pot Chemical Vapor Deposition Synthesis. *Adv. Funct. Mater.* **2021**, 31, 2101086.
[10.1002/adfm.202101086](https://doi.org/10.1002/adfm.202101086)
- [5] W. Yao, Z. Kang, J. Deng, Y. Chen, Q. Song, X. L. Ding, F. Lu, W. Wang, Synthesis of 2D MoS₂(1-x)Se_{2x} semiconductor alloy by chemical vapor deposition. *RSC Adv.* **2020**, 10, 42172-42177.
[10.1039/D0RA07776C](https://doi.org/10.1039/D0RA07776C)
- [6] Q. Feng, N. Mao, J. Wu, H. Xu, C. Wang, J. Zhang, L. Xie. Growth of MoS₂(1-x)Se_{2x} (x = 0.41–1.00) monolayer alloys with controlled morphology by physical vapor deposition. *ACS nano* **2015**, 9, 7450-7455.
[10.1021/acsnano.5b02506](https://doi.org/10.1021/acsnano.5b02506)
- [7] R. Ghosh, J. S. Kim, A. Roy, H. Chou, M. Vu, S. K. Banerjee, D. Akinwande. Large area chemical vapor deposition growth of monolayer MoSe₂ and its controlled sulfurization to MoS₂. *J. Mater. Res.* **2016**, 31, 917-922.
[10.1557/jmr.2016.7](https://doi.org/10.1557/jmr.2016.7)
- [8] Y. Gao, Z. Liu, D.-M. Sun, L. Huang, L.-P. Ma, L.-C. Yin, T. Ma, Z. Zhang, X.-L. Ma, L.-M. Peng, H.-M. Cheng, W. Ren, Large-area synthesis of high-quality and uniform monolayer WS₂ on reusable Au foils. *Nat. Commun.* **2015**, 6, 8569.
[10.1038/ncomms9569](https://doi.org/10.1038/ncomms9569)
- [9] Z. Tang, C. Neumann, A. Winter, A. Turchanin, Electrochemical delamination assisted transfer of molecular nanosheets. *Nanoscale* **2020**, 12, 8656-8663.
[10.1039/d0nr01084g](https://doi.org/10.1039/d0nr01084g)
- [10] T. Taniguchi, K. Watanabe, Synthesis of high-purity boron nitride single crystals under high pressure by using Ba–BN solvent. *J. Cryst. Growth* **2007**, 303, 525-529.
[10.1016/j.jcrysgro.2006.12.061](https://doi.org/10.1016/j.jcrysgro.2006.12.061)
- [11] A. Winter, A. George, C. Neumann, Z. Tang, M. J. Mohn, J. Biskupek, N. Masurkar, A. L. M. Reddy, T. Weimann, U. Hübner, U. Kaiser, A. Turchanin, Lateral

- heterostructures of two-dimensional materials by electron-beam induced stitching. *Carbon* **2018**, *128*, 106-116.
[10.1016/j.carbon.2017.11.034](https://doi.org/10.1016/j.carbon.2017.11.034)
- [12] G. Kresse, J. Hafner, Ab initio molecular dynamics for liquid metals. *Phys. Rev. B* **1993**, *47*, 558-561.
[10.1103/PhysRevB.47.558](https://doi.org/10.1103/PhysRevB.47.558)
- [13] G. Kresse, J. Furthmüller, Efficiency of ab-initio total energy calculations for metals and semiconductors using a plane-wave basis set. *Comput. Mater. Sci* **1996**, *6*, 15-50.
[10.1016/0927-0256\(96\)00008-0](https://doi.org/10.1016/0927-0256(96)00008-0)
- [14] J. P. Perdew, K. Burke, M. Ernzerhof, Generalized gradient approximation made simple. *Phys. Rev. Lett.* **1996**, *77*, 3865-3868.
[10.1103/PhysRevLett.77.3865](https://doi.org/10.1103/PhysRevLett.77.3865)
- [15] P. E. Blöchl, Projector augmented-wave method. *Phys. Rev. B* **1994**, *50*, 17953-17979.
[10.1103/PhysRevB.50.17953](https://doi.org/10.1103/PhysRevB.50.17953)
- [16] S. Grimme, Semiempirical GGA-type density functional constructed with a long-range dispersion correction. *J. Comput. Chem.* **2006**, *27*, 1787-1799.
[10.1002/jcc.20495](https://doi.org/10.1002/jcc.20495)
- [17] G. Henkelman, B. P. Uberuaga, H. Jónsson, A climbing image nudged elastic band method for finding saddle points and minimum energy paths. *J. Chem. Phys.* **2000**, *113*, 9901-9904.
[10.1063/1.1329672](https://doi.org/10.1063/1.1329672)
- [18] A.-Y. Lu, H. Zhu, J. Xiao, C.-P. Chuu, Y. Han, M.-H. Chiu, C.-C. Cheng, C.-W. Yang, K.-H. Wei, Y. Yang, Y. Wang, D. Sokaras, D. Nordlund, P. Yang, D. A. Muller, M.-Y. Chou, X. Zhang, L.-J. Li, Janus monolayers of transition metal dichalcogenides. *Nat. Nanotechnol.* **2017**, *12*, 744-749.
[10.1038/nnano.2017.100](https://doi.org/10.1038/nnano.2017.100)
- [19] Y. Guo, Y. Lin, K. Xie, B. Yuan, J. Zhu, P.-C. Shen, A.-Y. Lu, C. Su, E. Shi, K. Zhang, C. HuangFu, H. Xu, Z. Cai, J.-H. Park, Q. Ji, J. Wang, X. Dai, X. Tian, S. Huang, L. Dou, L. Jiao, J. Li, Y. Yu, J.-C. Idrobo, T. Cao, T. Palacios, J. Kong, Designing artificial two-dimensional landscapes via atomic-layer substitution. *Proc. Natl. Acad. Sci. U.S.A* **2021**, *118*, e2106124118
[10.1073/pnas.2106124118](https://doi.org/10.1073/pnas.2106124118)
- [20] D. B. Trivedi, G. Turgut, Y. Qin, M. Y. Sayyad, D. Hajra, M. Howell, L. Liu, S. Yang, N. H. Patoary, H. Li, M. M. Petrić, M. Meyer, M. Kremser, M. Barbone, G. Soavi, A. V. Stier, K. Müller, S. Yang, I. S. Esqueda, H. Zhuang, J. J. Finley, S. Tongay, Room-Temperature Synthesis of 2D Janus Crystals and their Heterostructures. *Adv. Mater.* **2020**, *32*, 2006320.
[10.1002/adma.202006320](https://doi.org/10.1002/adma.202006320)
- [21] Y.-C. Lin, C. Liu, Y. Yu, E. Zarkadoula, M. Yoon, A. A. Puretzky, L. Liang, X. Kong, Y. Gu, A. Strasser, H. M. Meyer, M. Lorenz, M. F. Chisholm, I. N. Ivanov, C. M. Rouleau, G. Duscher, K. Xiao, D. B. Geohegan, Low Energy Implantation into Transition-Metal Dichalcogenide Monolayers to Form Janus Structures. *ACS Nano* **2020**, *14*, 3896-3906
[10.1021/acsnano.9b10196](https://doi.org/10.1021/acsnano.9b10196)
- [22] B. Huang, F. Tian, Y. Shen, M. Zheng, Y. Zhao, J. Wu, Y. Liu, S. J. Pennycook, J. T. L. Thong, Selective engineering of chalcogen defects in MoS₂ by low-energy helium plasma. *ACS Appl. Mater. Interfaces* **2019**, *11*, 24404-24411.

- [10.1021/acsami.9b05507](https://doi.org/10.1021/acsami.9b05507)
- [23] J. Zhang, S. Jia, I. Kholmanov, L. Dong, D. Er, W. Chen, H. Guo, Z. Jin, V. B. Shenoy, L. Shi, J. Lou, Janus Monolayer Transition-Metal Dichalcogenides. *ACS Nano* **2017**, *11*, 8192-8198.
[10.1021/acsnano.7b03186](https://doi.org/10.1021/acsnano.7b03186)
- [24] H.-P. Komsa, A. V. Krashenninnikov, Two-Dimensional Transition Metal Dichalcogenide Alloys: Stability and Electronic Properties. *J. Phys. Chem. Lett.* **2012**, *3*, 3652-3656.
- [25] J. Mann, Q. Ma, P. M. Odenthal, M. Isarraraz, D. Le, E. Preciado, D. Barroso, K. Yamaguchi, G. von Son Palacio, A. Nguyen, T. Tran, M. Wurch, A. Nguyen, V. Klee, S. Bobek, D. Sun, T. F. Heinz, T. S. Rahman, R. Kawakami, L. Bartels, 2-Dimensional Transition Metal Dichalcogenides with Tunable Direct Band Gaps: MoS₂(1-x)Se_{2x} Monolayers. *Adv. Mater.* **2014**, *26*, 1399-1404.
[10.1002/adma.201304389](https://doi.org/10.1002/adma.201304389)
- [26] H.-J. Kim, D. Kim, S. Jung, M.-H. Bae, Y. J. Yun, S. N. Yi, J.-S. Yu, J.-H. Kim, D. H. Ha, Changes in the Raman spectra of monolayer MoS₂ upon thermal annealing. *J. Raman Spectrosc.* **2018**, *49*, 1938-1944.
[10.1002/jrs.5476](https://doi.org/10.1002/jrs.5476)
- [27] X. Wei, Z. Yu, F. Hu, Y. Cheng, L. Yu, X. Wang, M. Xiao, J. Wang, X. Wang, Y. Shi, Mo-O bond doping and related-defect assisted enhancement of photoluminescence in monolayer MoS₂. *AIP Adv.* **2014**, *4*, 123004.
[10.1063/1.4897522](https://doi.org/10.1063/1.4897522)
- [28] A. Turchanin, D. Käfer, M. El-Desawy, C. Wöll, G. Witte, A. Götzhäuser, Molecular mechanisms of electron-induced cross-linking in aromatic SAMs. *Langmuir* **2009**, *25*, 7342-7352.
[10.1021/la803538z](https://doi.org/10.1021/la803538z)
- [29] C. Neumann, R. A. Wilhelm, M. Küllmer, A. Turchanin, Low-energy electron irradiation induced synthesis of molecular nanosheets: influence of the electron beam energy. *Faraday Discuss.* **2021**, *227*, 61-79.
[10.1039/C9FD00119K](https://doi.org/10.1039/C9FD00119K)
- [30] V. I. Nefedov, Photoelectron elastic scattering effects in XPS. *J. Electron Spectrosc. Relat. Phenom.* **1999**, *100*, 1-15. [10.1016/S0368-2048\(99\)00037-7](https://doi.org/10.1016/S0368-2048(99)00037-7)
- [31] R. Sant, M. Gay, A. Marty, S. Lisi, R. Harrabi, C. Vergnaud, M. T. Dau, X. Weng, J. Coraux, N. Gauthier, O. Renault, G. Renaud, M. Jamet, Synthesis of epitaxial monolayer Janus SPtSe. *npj 2D Mater. Appl.* **2020**, *4*, 41.
[10.1038/s41699-020-00175-z](https://doi.org/10.1038/s41699-020-00175-z)
- [32] A. V. Naumkin, A. Kraut-Vass, S. W. Gaarenstroom, C. J. Powell, NIST Standard Reference Database 20. 4.1 ed; **2012**.
[10.18434/T4T88K](https://doi.org/10.18434/T4T88K)
- [33] S. Shree, I. Paradisanos, X. Marie, C. Robert, B. Urbaszek, Guide to optical spectroscopy of layered semiconductors. *Nat. Rev. Phys.* **2021**, *3*, 39-54
[10.1038/s42254-020-00259-1](https://doi.org/10.1038/s42254-020-00259-1)
- [34] Y. Qin, M. Sayyad, A. R.-P. Montblanch, M. S. G. Feuer, D. Dey, M. Blei, R. Sailus, D. M. Kara, Y. Shen, S. Yang, A. S. Botana, M. Atature, S. Tongay, Reaching the Excitonic Limit in 2D Janus Monolayers by In Situ Deterministic Growth. *Adv. Mater.* **2021**, *34*, 2106222.
[10.1002/adma.202106222](https://doi.org/10.1002/adma.202106222)

- [35] J. Schmeink, V. Musytschuk, E. Pollmann, S. Sleziona, A. Maas, M. Schleberger, Lifetime of Excitons in Janus Monolayer MoSSe Prepared from Exfoliated MoSe₂ <https://arxiv.org/abs/2112.11211>, **2021**.
- [36] I. Pelant, J. Valenta, *Luminescence Spectroscopy of Semiconductors*, Oxford University Press, Oxford, **2012**. [10.1093/acprof:oso/9780199588336.001.0001](https://doi.org/10.1093/acprof:oso/9780199588336.001.0001)
- [37] M. M. Glazov, E. L. Ivchenko, G. Wang, T. Amand, X. Marie, B. Urbaszek, B. L. Liu, Spin and valley dynamics of excitons in transition metal dichalcogenide monolayers. *Phys. Status Solidi B* **2015**, 252, 2349-2362. [10.1002/pssb.201552211](https://doi.org/10.1002/pssb.201552211)
- [38] S. H. Su, W. T. Hsu, C. L. Hsu, C. H. Chen, M. H. Chiu, Y. C. Lin, W. H. Chang, K. Suenaga, J. H. He, L. J. Li, Controllable synthesis of band-Gap-Tunable and Monolayer Transition-Metal Dichalcogenide Alloys. *Front. Energy Res.* **2014**, 2, 27. [10.3389/fenrg.2014.00027](https://doi.org/10.3389/fenrg.2014.00027)